Optical Flow For Image-Based River Velocity Estimation

Musaab Khalid, Lionel Pénard, Etienne Mémin

Optical Flow For Image-Based River Velocity Estimation

M. Khalid, L. Pénard, E. Mémin

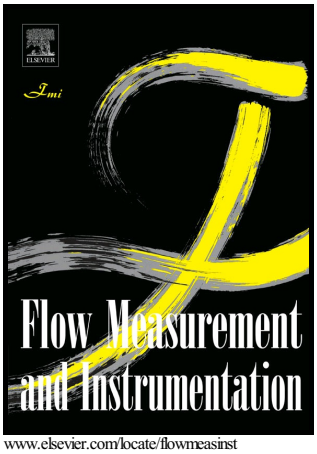

www.elsevier.com/locate/flowmeasinst

PII: S0955-5986(18)30026-8
DOI: https://doi.org/10.1016/j.flowmeasinst.2018.11.009
Reference: JFMI1501

To appear in: *Flow Measurement and Instrumentation*

Received date: 22 January 2018
Revised date: 8 September 2018
Accepted date: 10 November 2018

Cite this article as: M. Khalid, L. Pénard and E. Mémin, Optical Flow For Image-Based River Velocity Estimation, *Flow Measurement and Instrumentation,* https://doi.org/10.1016/j.flowmeasinst.2018.11.009

Optical Flow For Image-Based River Velocity Estimation

M. Khalid[a], L. Pénard[a], E. Mémin[b]

[a] *Irstea, UR RiverLy, centre de Lyon-Villeurbanne, 5 rue de la Doua CS 20244, 69625 Villeurbanne, France*
[b] *Fluminance, Inria/Irstea/IRMAR, Campus de Beaulieu, 35042 Rennes, France*

Abstract

We present a novel motion estimation technique for image-based river velocimetry. It is based on the so-called *optical flow*, which is a well developed method for rigid motion estimation in image sequences, devised in computer vision community. Contrary to PIV (Particle Image Velocimetry) techniques, optical flow formulation is flexible enough to incorporate physics equations that govern the observed quantity motion. Over the past years, it has been adopted by experimental fluid dynamics community where many new models were introduced to better represent different fluids motions, (see (Heitz et al., 2010) for a review). Our optical flow is based on the scalar transport equation and is augmented with a weighted diffusion term to compensate for small scale (non-captured) contributions. Additionally, since there is no ground truth data for such type of image sequences, we present a new evaluation method to assess the results. It is based on trajectory reconstruction of few Lagrangian particles of interest and a direct comparison against their manually-reconstructed trajectories. The new motion estimation technique outperformed traditional optical flow and PIV-based methods.

Keywords: Optical Flow, River Velocimetry, PIV, LSPIV

1. Introduction

To estimate the velocity of the free surface of a river using image-based techniques, there are two main issues to be addressed. The first is the 2D motion estimation in image space and the second issue is about how to transform 2D image estimations back to 3D. It should also handle the scaling of these estimations to their true physical scale. The metric surface velocity could be then obtained using the time between images. It is a valuable piece of information to compute rivers discharge using the well-known *velocity-area* method. The work presented here focuses on the first issue. We specifically target rivers with noticeable discharge or urban inundations. In these settings, the free surface manifests a visible and probably turbulent translatory motion.

For many years, PIV (Particle Image Velocimetry) (Adrian, 1991) was the only technique available for fluid motion estimation in image sequences. PIV computes the

displacement between windows of a certain size in two consecutive images depicting spatio-temporal evolution of a fluid. These windows are tracked assuming a translational motion between images using some measure of similarity that is computed on them. To compute better similarity scores, the flow has to be well-seeded with particles. As a consequence, PIV faces strong difficulties on scalar images in which many areas have low intensity gradient. In many cases, there is a necessary post-processing step to correct or remove spurious vectors, inevitably generated in regions with low intensity gradient. The post-processing step is also used to interpolate the sparse vector field to generate a denser one. In addition, choosing a suitable window size is a tricky task, one needs bigger window to accumulate more information for better score computation, but then the bigger the window, the more likely it contains complex motions far from the window's translational motion assumption. Despite its wide-spread usage specially in controlled lab environments, PIV lacks sound physics foundation, it treats all image sequences equally, regardless of the nature of the object in motion. Furthermore, it only computes sparse estimations, many of them might be discarded in the post-processing phase. In their seminal paper, Fujita et al. (1998) took PIV outside the lab to measure the velocity of rivers in *ortho-rectified* image sequences. The ortho-rectification applies geometric transformation to produce new set of images in which the perspective effect is removed. The ortho-rectified sequence is produced in such a way that their real spatial resolution is now known. The image motion estimation technique (PIV in this case) is then applied to the newly created sequence. Hence, the name of their method LSPIV (Large Scale Particle Image Velocimetry) which became the benchmark for image-based river velocimetry (Jodeau et al., 2008, Dramais et al., 2011, Muste et al., 2014).

If we closely examine the original problem as depicted in Figure (1.1), the motion in 3D space is captured by a camera and as a result, a 2D motion is observed in images. The image-based velocimetry problem is exactly solved by taking the reverse route. We can distinguish the two aforementioned issues or steps that need to be solved along this route. Most LSPIV works however mix the two steps together which makes it difficult to determine the exact sources of uncertainty and the effects of each step error to the overall error. It is a valid idea to take the route shown by the blue arrows in Figure (1.1) and treat each issue individually. Recently, Patalano et al. (2017) applied the ortho-rectification only to the results but the motion estimation was separately applied to the original obliquely-viewed images. This paper focuses only on the first step, that is, motion estimation of river surface in image space.

Due to PIV limitations cited above, we found the so-called *Optical Flow* (Horn and Schunck, 1981) to be well adapted to fluids. A nice review paper on the application of optical flow to fluids could be find in (Heitz et al., 2010).

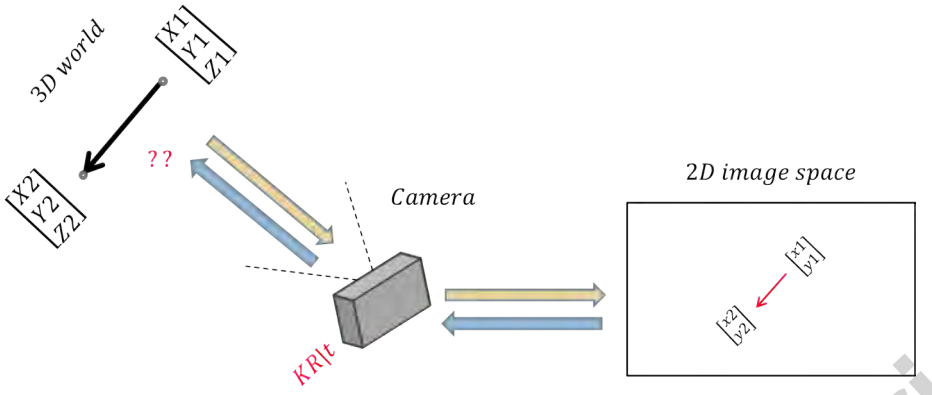

Figure 1.1: 3D motion projection to images.

Previous work

Stemmed from computer vision community in the early 80s due to Horn and Schunck (1981) work. Optical flow consists of an energy functional to be minimized. It combines the information that could be extracted from images (called data term) and the expected solutions set (called regularization term) in a concise and unambiguous way:

$$\int_{\Omega} \left(\frac{\partial I}{\partial t} + \nabla I \cdot \omega \right)^2 + \alpha \left\| \nabla \omega \right\|^2 dX \tag{1.1}$$

where ∇ represents the spatial gradient for both image intensity function I and the 2D velocity field $\omega = [u, v]$. A parameter α is introduced to define the trade-off between the data term and the regularization term. The first quadratic term (data term) is called the *brightness constancy* (BC). It assumes that points conserve their brightness value captured by the camera while moving in a small time interval. The second term is trying to minimize velocity gradient globally, assuming that neighbouring points belong normally to the same surface and tend to move together. This assumption resembles the one made in PIV that *all* points in the window have the same velocity. However, its formulation in optical flow is more relaxed, velocities of points on the same neighbourhood could vary, but this variation should be limited. This model witnessed many improvements over the years to overcome its limitations.

First of all, the BC assumption used in the data term in (1.1) is derived using Taylor approximation to linearize the original non-linear pattern matching BC, $I(X(t), t) = I(X(t+1), t+1)$. The linearized model assumes very small motion which is indeed not the case in general. To deal with large displacements, the use of different image resolutions in a hierarchical, coarse-to-fine way (called image pyramid) has been introduced (Bergen et al., 1992). This strategy is improved by using

warping steps in which the second image is brought *closer* to the first image using the estimated velocity field of the previous pyramid level (Mémin and Pérez, 1998, 2002). Consequently, only a small increment is sought at each level.

Secondly, the quadratic penalization is known to be sensitive to outliers. This is particularly seen in image regions with discontinuities where we might have two different objects moving in different directions at different speeds. The quadratic penalization tends to average these two motions which results in a solution clearly not in agreement with the real motion at the discontinuity area and around it. Black and Anandan (1996) proposed to use robust penalization methods to cope with outliers. This procedure gave better results i.e. sharper discontinuities.

Lastly, the BC assumption might not hold in many cases due to occlusions, imaging acquisition quality and/or illumination changes caused by surface reflections for instance. Therefore, it is a good practice to use a robust function for the data term as well (Mémin and Pérez, 1998). Other notable improvements were proposed by Mémin and Pérez (1998), Brox et al. (2004) in which authors used the original non-linear version of BC. The resulting non-linear equation is solved iteratively using a multi-grid optimization technique (Mémin and Pérez, 1998) or a Graduated-Non-Convexity (GNC) (Blake and Zisserman, 1987) with two fixed point iterations optimization technique. Median filtering of intermediate flow (between pyramid levels) showed very good performance regarding outliers rejection. Sun et al. (2014) elaborated on this and showed that it is a different energy function when median filtering is utilized.

The functional (1.1) was designed for rigid or quasi-rigid motions as they are the most encountered in natural scenes. Fluids in general have more complex motion patterns. Liu and Shen (2008) formally established the relationship between optical flow and fluid flow based on the perspective projection of the transport equation on the 2D plane and found that optical flow is proportional to the path-averaged velocity field weighted with a relevant field quantity. This gave the physical foundation needed since the BC assumption is not based on any physical principle. Higher order regularization has been proposed before by Suter (1994) based on the divergence and the curl of the vector field. However, minimizing such high order terms is known to be problematic. Corpetti et al. (2005) proposed a relaxed and easier term to minimize the gradient of divergence and curl. They also suggested a data term based on the *Integrated Continuity Equation*. They also showed that, from an optimization point of view, the L_2 regularization in equation (1.1) is equivalent to penalizing divergence and curl equally, which might be a problem depending on the fluid at hand. Heitz et al. (2008) suggested to refrain from multi-resolution strategy for PIV applications because the smoothing and sub-sampling of images will suppress the particles in the coarsest resolution levels. They introduced a model that combines local information (PIV) with a global dense optical flow formulation. A very promising line of research consists of deriving new data term based on LES (Large Eddy Simulation) of the transport equation (Cassisa et al., 2011, Chen et al., 2015). The latter used a divergence norm penalization term as regularization to conserve the curl of the vector field. This derivation from transport equation separates the effects of information

captured on the image pixels' grid and the contribution of the small non-captured scales (subgrid). This paper belongs to this line of research and proposes a simple way to model the small scales contribution in river flows.

In section 2 we present the necessary derivation for the optical flow data term followed by the regularization term in section 3. In section 4, we detail how the energy functional is discretized and minimized. An evaluation of the model is done on image sequences of rivers with comparisons against conventional optical flow model and PIV/LSPIV is presented in section 5. We then conclude in section 6. This paper extends and elaborate in greater details a previous work published at a conference (Khalid et al., 2017). Main differences amongst others consist of an implementation section that makes the paper more self-contained, direct comparison with LSPIV on ortho-rectified images, rigorous parameters fine-tuning and more results and image sequences.

2. Data term

For the specific case of rivers sequences, we make the assumption that the image intensity function I is related to some passive scalar field concentration C. They are related by a perspective transformation that projects a real world quantity into the observed image plane forming the intensity function I. Let us examine the scalar transport equation:

$$\frac{\partial C}{\partial t} + \nabla \cdot (C\omega) - \frac{1}{Re\, Sc}\Delta C = 0 \tag{2.1}$$

where $\nabla\cdot$ is the divergence operator, Δ is the Laplacian operator, Re and Sc are the *Reynolds* and *Schmidt* numbers, respectively. The transport equation above links the scalar quantity C to the sought velocity vector field ω. However, in order to be able extract the velocity, the function C has to contain information till *Kolmogorov* scale. Since C is captured by a camera, the pictured image corresponds indeed to a smooth filtered version of the scalar quantity. It is hence a large-scale representation of the scalar in which the small-scale contributions are omitted. In the case of fluid flows the small-scale effects can not be neglected. Their action on the large-scale drift component must be modeled (Cui et al., 2007). Following (Cassisa et al., 2011, Chen et al., 2015), we propose a LES (Large Eddy Simulation) decomposition of the transport equation to model the small scales contributions in river sequences. The expression $\nabla \cdot (C\omega)$ could be divided into an observed $(\nabla \cdot (I\omega))$ and non-observed $(\nabla \cdot (\tau))$ parts, leading to:

$$\frac{\partial I}{\partial t} + \nabla \cdot (I\omega) + \nabla \cdot (\tau) - \frac{1}{Re\, Sc}\Delta I = 0 \tag{2.2}$$

in image space. The molecular diffusion term $\frac{1}{Re\, Sc}\Delta I$ is normally neglected. We also assume that the incompressibility condition for water still holds on the 2D plane (that the divergence of the 2D velocity field is zero). When applying the incompressibility condition and ignoring the molecular diffusion term, equation 2.2 becomes:

$$\frac{\partial I}{\partial t} + \nabla I \cdot \omega + \nabla \cdot (\tau) = 0 \tag{2.3}$$

We see that the BC assumption appears again in addition to the new subgrid term, which means conventional optical flow is consistent with this physics-based derivation. As suggested by Cassisa et al. (2011), the non-observed term is considered related to turbulent viscosity $\tau = -D_t \nabla I$ where D_t is a turbulent diffusion coefficient. We opted for a simple model to estimate D_t using previous velocity estimations within the sequence and/or the pyramid levels of image pair at hand. We feed these velocity estimations to *Prandtl* mixing-length model (Prandtl, 1925). This model uses the streamwise velocity u and the Mixing Length l to estimate the turbulent viscosity $\nu_t = l^2 \left| \frac{du}{dy} \right|$. This quantity is relevant for the computation of $D_t = \frac{\nu_t}{sc_t}$ where sc_t is the *turbulent Schmidt number* which has an empirical value usually determined experimentally. It has been reported that sc_t has widespread values between 0.2 and 3 in general (Tominaga and Stathopoulos, 2007) while other authors very recently suggested values around 1 to be optimal on a tracer transport study (Gualtieri et al., 2017). Accordingly, D_t is considered equal to ν_t. The Mixing Length l is defined as the distance traversed by a fluid parcel before it becomes blended in with neighbouring masses. To the best of our knowledge, there is no clear way to predict this value from images. It is taken here to be 1 because the differential optical flow formulation assumes infinitesimal displacements that don't exceed one pixel.

Due to sources or sinks in the fluid, the imaged surface is prone to intermittent changes because of out of plane (depth) motions. Some regions may rise up or sink down during the temporal evolution of the fluid causing changes in the intensity function. As a result, the brightness consistency assumption might not hold in many locations. Thus, a robust function is chosen for the data term. In practice we mainly use the Lorentzian function (Black and Anandan, 1996) but there are many others that could be used. The data term reads:

$$\int_\Omega \Psi \left(\left\| \frac{\partial I}{\partial t} + \nabla I \cdot \omega + \nabla \cdot (-D_t \nabla I) \right\|^2 \right)$$

where Ψ is the robust function. This could be further simplified as:

$$\int_\Omega \Psi \left(\left\| \frac{\partial I}{\partial t} + \nabla I \cdot \omega - D_t \Delta I \right\|^2 \right) \tag{2.4}$$

which is the proposed data term.

3. Regularization

Regarding the regularization, two main choices were made. Firstly, it can be noticed that usually the river flows of interest do not exhibit strong large-scale eddies motion. Rivers with such eddies have indeed less interest in river velocimetry

applications. There might be however many small scale vortices but due to river velocity and/or image acquisition speed, most of them are transported by the large-scale quasi-translational motion. As a result, we opted for a first order gradient penalization like in functional (1.1). As stated earlier, this regularization penalizes the divergence and the curl of the flow field equally. On the one hand, penalizing the divergence is beneficial to enforce the 2D incompressibility assumed. On the other hand, penalizing a non existent or a weak property like the curl will reject all solutions with strong vorticity. For the case of floods image sequences, their strong translatory nature does not promote chaotic motions. In other words, the turbulence does not occur at individual pixels. There is always this notion of groups of pixels that move together and in which case this regularization is optimal. In addition, in uniform intensity areas, the image intensity gradient diminishes and it is the regularization that takes the lead over the data term since the latter depends on image gradient. These uniform areas should then be moving together for this regularization to be relevant. We argue that in uniform intensity image areas, it is unlikely to have very different motions, otherwise, because of water and flow properties including velocity, there would be a mixing phenomenon that would eventually disrupt the uniformity of the intensity function in that specific area. The reverse logic should apply, if the area is uniform in intensity, it is more likely that it contains similar velocity vectors i.e. points move together, in which case this regularization is definitely optimal. The second choice made is to take a quadratic function instead of robust one for the regularization. The reasoning behind this is: previously robust functions are utilized in the regularization of rigid motion sequences to improve the results on discontinuities, these discontinuities are due to different objects motions and/or different depth differences, etc... However, there is only one object of interest here, which is the river water surface. Though complex, its underlying motion is not discontinuous and there is no reason to introduce penalty terms enforcing the apparition of discontinuities between two adjacent points. The quadratic functions behavior is exactly suitable in this prospect as it tends to average the two different motions in the neighbourhood of interest. The regularization reads:

$$\int_{\Omega} \alpha \left\| \nabla \omega \right\|^2 dX$$

The final model equation after combining the two terms is:

$$E(\omega) = \int_{\Omega} \Psi \left(\left\| \frac{\partial I}{\partial t} + \nabla I \cdot \omega - D_t \Delta I \right\|^2 \right) + \alpha \left\| \nabla \omega \right\|^2 dX \tag{3.1}$$

We name the model SGSD (SubGrid Scale Diffusion).

4. Implementation

In practice, the original non-linear displacement model i.e. $I(X(t+1), t+1) - I(X(t), t)$ is utilized in a coarse-to-fine fashion with warping as in (Brox et al., 2004,

Mémin and Pérez, 1998). Not only to allow the estimation of large displacements, but also because the diffusion coefficient D_t depends on the velocity computed on previous coarser pyramid level. The linear BC used earlier is only a Taylor approximation to this model while assuming small motions. The velocity vector field is initialized using conventional optical flow at the coarsest level (which in its turn initialized by a zero-valued vector field). The estimated vector field is propagated to the next finer level after applying the necessary scaling. The vector field is then used to warp the second image of the finer level towards the first image of the same level. Only a small increment of the vector field is sought at this level $\omega^{k+1} = \omega^k + d\omega^{k+1}$, implying that we already know ω^k and we look only for the increment $d\omega^{k+1}$. Equation (3.1) could be minimized using Euler-Lagrange equations. However, an Iterative Reweighted Least Squares IRLS approach, previously used by Mémin and Pérez (1998), is equivalent to the variational Euler-Lagrange as shown by Liu (2009), yet simpler to derive while working on the discrete equivalent of equation (6). Let

$$
\begin{aligned}
I_t &= I(X+\omega) - I(X), \\
I_x &= \frac{\partial}{\partial x} I(X+\omega), \\
I_y &= \frac{\partial}{\partial y} I(X+\omega)
\end{aligned}
$$

Since we have introduced $d\omega$ earlier, an expression of an incremental BC $I(X+\omega+d\omega) - I(X)$ could be linearized using Taylor expansion as:

$$
I_t + I_x du + I_y dv \tag{4.1}
$$

where $d\omega = (du, dv)$. Equation (4.1) is equivalent to the linear BC in equation (1.1) but it is derived on a pyramid level after warping. The difference of this approach with original Horn and Schunck (HS) optical flow is that while both rely on a linearized expression, for HS this linearization is applied only once. While in equation (4.1) the linearization is performed successively on every pyramid level at least once. The discretized version of equation (3.1) applied at a given pyramid level reads:

$$
\begin{aligned}
E(du, dv) = \sum_X \Psi \left(\delta_X^T \left(I_t + I_x du + I_y dv - D_t \left(\triangle I \right) \right)^2 \right) + \\
\alpha [\left(\delta_X^T F_x \left(u + du \right) \right)^2 + \left(\delta_X^T F_y \left(u + du \right) \right)^2 + \\
\left(\delta_X^T F_x \left(v + dv \right) \right)^2 + \left(\delta_X^T F_y \left(v + dv \right) \right)^2]
\end{aligned} \tag{4.2}
$$

where δ_X^T is a column vector with all zeros except on the position X and $F_*; {}_*\epsilon \{x, y\}$ are derivative filter matrices in the direction of the subscript. u, v, du and dv are all vectorized and $I_*; {}_*\epsilon \{x, y, t\}$ are all diagonalized, for instance $diag[I_x]$. The goal is to find du and dv that minimizes the gradient $\left[\frac{dE}{\partial du}; \frac{dE}{\partial dv} \right] = 0$. Using matrix calculus we have:

$$\frac{\partial E}{\partial du} = 2\sum_{X} \Psi^{'}\left(I_x\delta_X\delta_X^T I_x du + I_x\delta_X\delta_X^T\left(I_t + I_y dv - D_{t,u}\Delta I\right)\right) + \left(F_x^T\delta_X\delta_X^T F_x + F_y^T\delta_X\delta_X^T F_y\right)(u + du) \tag{4.3}$$

where $\Psi^{'}$is the derivative of the robust function with respect to its parameters. Since $\delta_X\delta_X^T$ will add up to identity, some arrangement of the terms will yield:

$$\frac{\partial E}{\partial du} = 2\left(\left(\Psi^{'} I_x^2 + \alpha L\right)du + \Psi^{'} I_x I_y dv + \Psi^{'}\left(I_x I_t - I_x(D_{t,u}\Delta I)\right) + \alpha L u\right) \tag{4.4}$$

where L is a Laplacian filter defined as $F_x^T IDF_x + F_y^T IDF_y$, ID being the identity matrix. The identity here comes from the quadratic function, if we use a robust function, we would have a diagonal matrix composed of the robust weights instead. An equation for dv could be obtained in the same way.

$$\frac{\partial E}{\partial dv} = 2\left(\Psi^{'} I_x I_y du + \left(\Psi^{'} I_y^2 + \alpha L\right)dv + \Psi^{'}\left(I_y I_t - I_y(D_{t,v}\Delta I)\right) + \alpha L v\right) \tag{4.5}$$

The only unknowns beside dv and du are the two turbulent diffusion coefficients, these could now be simply estimated using previous velocity estimates

$$\begin{aligned} D_{t,u} &= \left|\frac{\partial}{\partial y}u\right| \\ D_{t,v} &= \left|\frac{\partial}{\partial x}v\right| \end{aligned} \tag{4.6}$$

IRLS procedure considers the derivative of the robust function as a weight to an ordinary least squares problem. The convergence is achieved when no significant changes are observed in the weights or when a maximum number of iteration is reached. Two fixed point iterations are finally performed. In the inner loop, we solve for du and dv while continuously linearizing the non-linear model and updating the weight $\Psi^{'}$as shown in Algorithm 1. On convergence, the outer loop updates u and v and warp again the second image towards the first using the updated vector field. The final linear operator reads:

$$\begin{bmatrix} \Psi^{'} I_x^2 + \alpha L & \Psi^{'} I_x I_y \\ \Psi^{'} I_x I_y & \Psi^{'} I_y^2 + \alpha L \end{bmatrix}\begin{bmatrix} du \\ dv \end{bmatrix} = -\begin{bmatrix} \Psi^{'}\left(I_x I_t - I_x(D_{t,u}\Delta I)\right) + \alpha L u \\ \Psi^{'}\left(I_y I_t - I_y(D_{t,v}\Delta I)\right) + \alpha L v \end{bmatrix} \tag{4.7}$$

As in (Brox et al., 2004, Sun et al., 2014), we use a *continuation* method called Graduated Non Convexity (GNC) (Blake and Zisserman, 1987) to minimize the energy function. The general idea behind it is that the solution of a smoothed version of

Algorithm 1 Computation of optical flow on a pyramid level

```
for i = 1 to the max number of warping steps do
    Compute D_{t,u} and D_{t,v} as in equation (4.6) using current u and v
    Warp the second image towards the first using current u and v.
    Initialize du , dv to zero
    for j = 1 to max number of linearization steps do
        Linearize the problem using equation (4.1)
        Compute the weight Ψ'.
        Solve for du and dv using equation (4.7)
    end for
    update u and v using du and dv
end for
```

the problem represents a good initialization to solve the original problem. In practice, since we are dealing with a complicated optimization problem, the problem is firstly convexified using the quadratic formulation and then it is linearly and gradually changed until the original problem formulation. The energy function to be minimized is obtained using:

$$cE_Q + (1 - c)\, E_R \tag{4.8}$$

where $c \,\epsilon\, [0, 1]$, E_Q is the convex quadratic approximation of the problem, E_R is the robust and possibly non convex original problem. The whole process is depicted in Figure (4.1).

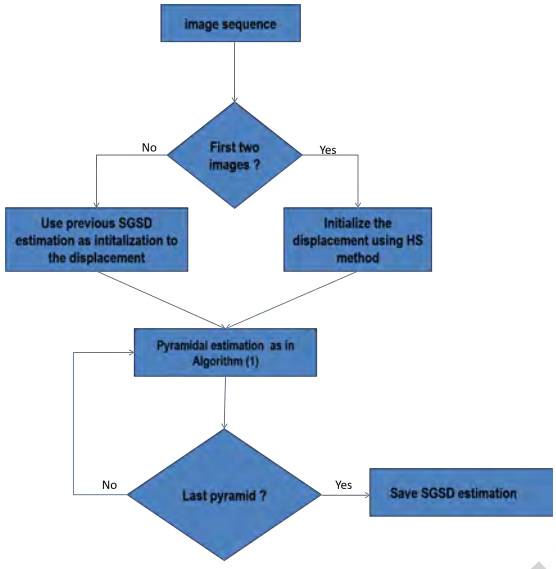

Figure 4.1: A flowchart describing SGSD estimation cycle.

5. Evaluation

One of the key factors of the maturity of optical flow approaches ensues from the availability of ground truth data. Authors compete in benchmarks such as Middlebury (Baker et al., 2011) and MP Sintel (Butler et al., 2012) to evaluate their models. When optical flow was borrowed by experimental fluid dynamics community, similar datasets were required while considering the governing physics equations. A reference simulation based on Navier-Stokes equations is used to generate such images using the simulated (and hence, known) velocity fields (Carlier and Wieneke, 2005). For river sequences however, a 3D simulation that respects the physics of rivers and then generate realistic 2D image sequences from it is a tedious job to do. Instead a simple idea has been utilized in this work to generate ground truth data. The idea is to track particles on Lagrangian basis throughout the sequence. First, a map of reference trajectories is obtained by tracking these particles manually. The manual tracking is performed at pixel-level (after zooming) using CellTracker free software (Piccinini et al., 2016). The error related to manual selection depends on the quality of the images. The error in the sequences we used in this study is about 1-2 pixel maximum in the transverse direction. On the longitudinal direction, the error is 1-2 pixels maximum for high quality images and 2-3 for degraded ones. Generally, we select the brightest pixel within a group of pixels that forms the particle. Figure (5.1) shows the location of a chosen particle in the original image and the same particle after zooming in two different images within the sequence. Then, integrating in time (through a 4th order Runge-Kutta), we reconstruct trajectories starting from the same initial points from the estimated displacement fields. The reconstructed

trajectories are then compared to their reference trajectories.

Figure 5.1: Manual tracking of particles: The position of the particle in the first image (top). Brightest position is chosen on pixel level after zooming in two different images (bottom).

We test the approach on different image sequences. The sequences differ mainly in their displacement magnitude, image quality, density of tracers (if any) and surface perturbations. The reference trajectories were reconstructed up to few pixels uncertainty. This is because particles change their orientations while moving and their form change as well when they are partially (or sometimes fully) occluded by water. We compare our method SGSD to a modified (Horn and Schunck, 1981) variation (HS). In fact, (HS) method used here is exactly the same as SGSD but does not include the turbulent diffusion term. A PIV-based method (Ray, 2011) that is capable of producing dense vector fields (necessary for trajectory reconstruction) is also compared to the two previous methods.

We use the same parameters for SGSD and for (HS) to highlight the difference of results with and without the diffusion term. Some of the aforementioned parameters are general and related to optical flow itself. For instance we use only two-stages GNC iterations in general. Additional GNC iterations improved the results for sequences with good seeding. Median filtering is another parameter to be considered. In general it is well-suited for sequences with less turbulence. If applied to turbulent sequences it might reject turbulent (but maybe correct) vectors and considers them as outliers. However, we found using it only between GNC iterations (and not between image pyramids) to be beneficial in all cases. The weighting factor between the data term and the regularization term is chosen as 0.6 for all sequences. We found that in general, the Lorentzian robust function works best for "good sequences". For noisy sequences or for those for which the 2D divergence assumption does not hold, the "Charbonnier" robust function (Charbonnier et al., 1994) gives slightly better results than the Lorentzian. We compute the normalized distance error of trajectories of different methods and also for SGSD with different Sc_t values:

$$Error(i) = \sqrt{\frac{\left((y(i)_{ref} - y(i))^2 + (x(i)_{ref} - x(i))^2\right)}{\sqrt{\left((y(1)_{ref} - y(end)_{ref})^2 + (x(1)_{ref} - x(end)_{ref})^2\right)}}}$$

where ref subscript refers to a reference trajectory component. We chose to normalize the error because we have different displacement values for different sequences. Note that smaller value for Sc_t means larger diffusion coefficient and vice versa. We also exploit the dense nature of the estimation to compute relevant differential operators in a straightforward way.

5.1. Results on conventional images

We collect videos of rivers in motion from various sources like YouTube or from research institutes data repositories. We require a *fixed* camera to make sure the motion is only due to the river. We also require the existence of at least few particles for the purpose of evaluation. The chosen particles are selected in such a way that they stay visible (at least partially) throughout the sequence.

5.1.1. The Arc river first sequence

The Arc river, located in the french Alps, is known for its dark color water which enhances the contrast (the gradient) of the image intensity when coupled with white tracers. In addition, the image quality itself is good with no changes in scene lighting. The sequence has 41 images. The average displacement in the streamwise direction is approximately 11 pixels between two images. In Figure (5.2), we plot the mean SGSD dense vector field (with an offset of few pixels for visualization purposes). This gives a quick spatio-temporal idea on the nature of the river at hand. Next, we plot the trajectories of different methods along the reference trajectory. In Figure (5.3, top), it is easy to observe that all methods were generally in agreement with the reference trajectory. This is mainly because of the good gradient signal in this sequence as mentioned earlier, but also to the quality of the images. Two zoomed areas around the middle and the end of the trajectory are shown. SGSD is almost identical to the reference trajectory, followed by (HS) and then PIV which appears to underestimate the motion magnitude. The zoomed window at the end of the trajectory confirms the results on the zoomed window in the middle (any false positive match in the middle will eventually result in a visible underestimation or overestimation in the window at the end). The normalized distance error in Figure (5.3, middle) confirms the results. In Figure (5.3, bottom) we plot the normalized distance error of SGSD using different values for Sc_t. This did not change the results much, there is a maximum error of 0.015 for the case with no diffusion and around 0.05 for other cases with different diffusion coefficients. Still SGSD with $Sc_t = 1$ gives the best results. In Figure (5.4, left), we take advantage of the dense estimation to compute a fine-detailed divergence field. In the same figure on the right, we could compute trajectories on an image cross-section. Observe that these trajectories do not necessarily start at a particle location like the one in Figure (5.3, top). Nevertheless, they are consistent with each other and specially to the ones that start at a particle location.

Figure 5.2: Mean dense SGSD velocity field of Arc river first sequence

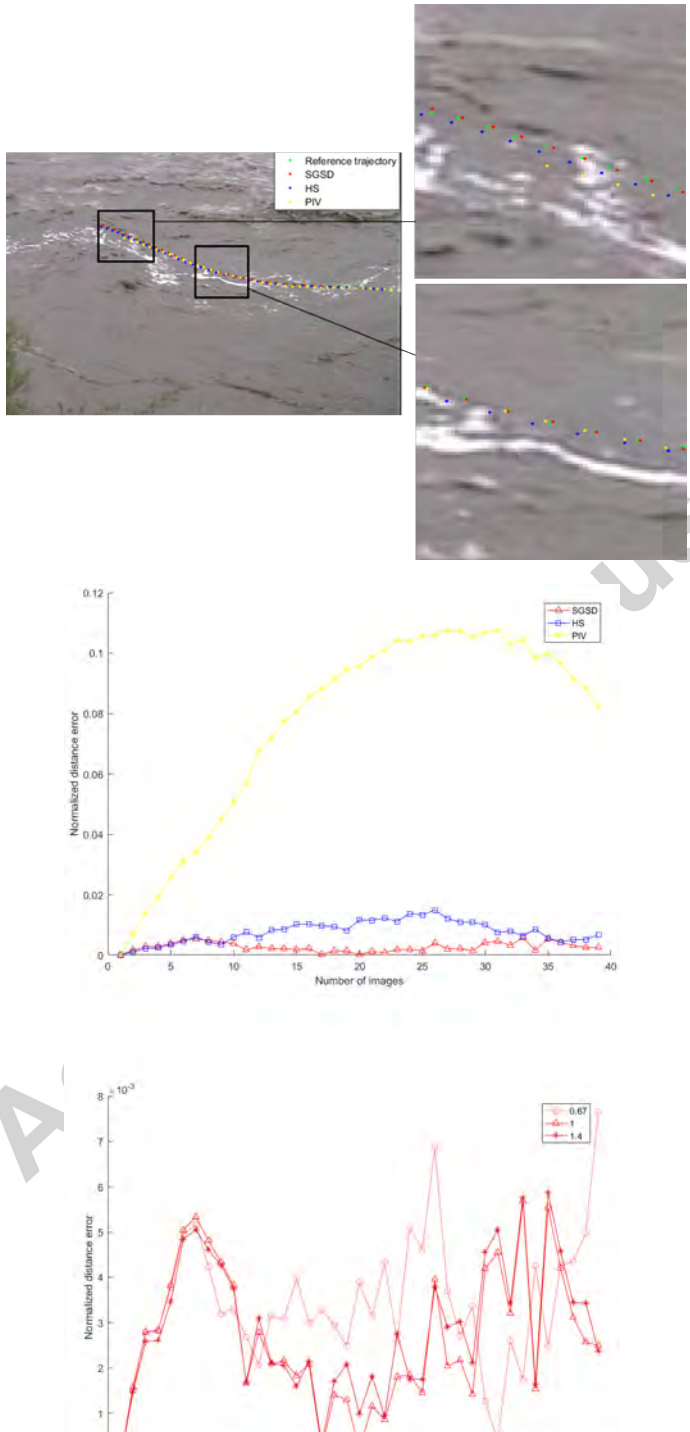

Figure 5.3: The trajectories of different methods superimposed on the first image of Arc river first sequence (top). Normalized distance error of different methods (middle). Normalized distance error of SGSD with different turbulent Schmidt numbers (bottom)

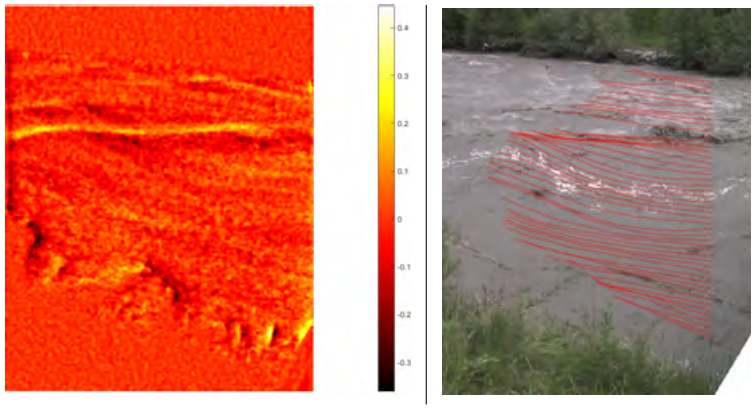

Figure 5.4: Other relevant quantities derived from SGSD for Arc river first sequence: divergence of the mean vector field (left). Trajectories on a cross-section (right)

5.1.2. The Arc river second sequence

In contrast to the first Arc sequence above, the imaging quality of this sequence is degraded. The tracked particle is very small which made even the manual tracking difficult. The sequence is composed of 55 images and the average displacement between two images is approximately 9 pixels. In Figure (5.5), the mean SGSD vector field is superimposed on one of the images. One could notice non-zero vectors in the non-fluid area in the bottom left part of the image. These are due to the wind moving the grass and not due to estimation errors. In Figure (5.6, top) we can see that SGSD was able to recover a better vector field in terms of magnitude and direction than PIV. With (HS), both vector fields seem to have the same magnitude, SGSD however was able to recover much better direction. In the same figure, we show the normalized distance error of different methods (middle) and for SGSD using different values for Sc_t (bottom). A larger diffusion coefficient gives better results. However, after 40 images it starts to diverge completely to a poor result with approximately 0.13 normalized error. The default SGSD with $Sc_t = 1$ is more stable throughout the whole sequence and most of the time better than the other two cases of no diffusion (HS) or with a small diffusion coefficient. Figure (5.7, left) shows the derived divergence field and cross-section trajectories are shown in the same figure on the right side. Contrary to the previous sequence, there is no clear visible tracers but the trajectories are still consistent.

Figure 5.5: Mean dense SGSD velocity field of Arc river second sequence

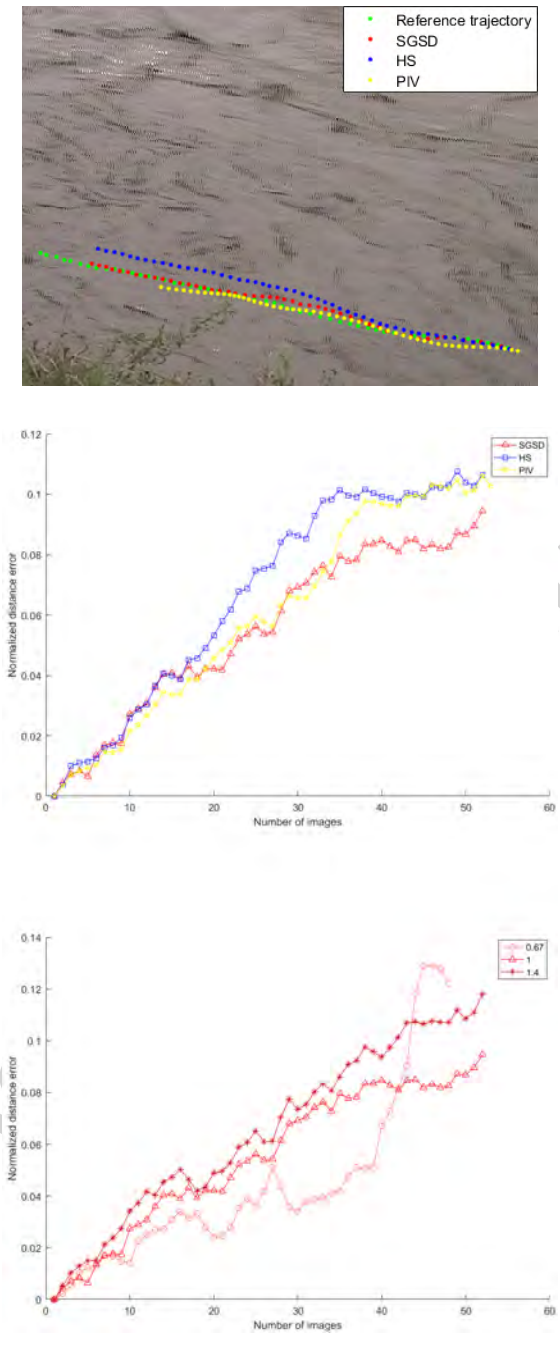

Figure 5.6: The trajectories of different methods superimposed on the first image of the Arc river second sequence (top). Normalized distance error of different methods (middle). Normalized distance error of SGSD with different turbulent Schmidt numbers (bottom)

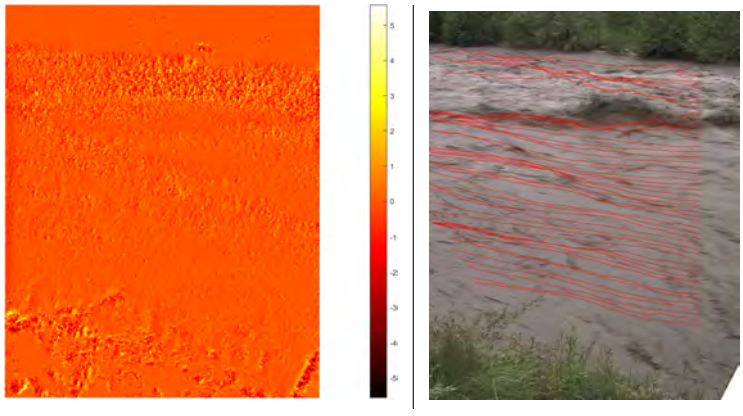

Figure 5.7: Other relevant quantities derived from SGSD for Arc river second sequence: divergence of the mean vector field (left). Trajectories on a cross-section (right)

5.1.3. The Gave de Pau river sequence

The Gave de Pau river, located in the french Pyrenees, is more challenging than the previous cases. The sequence has many uniform regions with weak gradient signal. Furthermore, the tracked particle is too big in size which increases the uncertainty of the reference trajectory reconstruction. This is because many pixels in the vicinity of the original selected pixel resemble each other. In addition, the river area where the particle resides (and a great deal of other parts) suffered from severe and persistent 3D motion which causes the particle to move up and down for extended period of time. This clearly violates the 2D incompressibility condition used to derive the optical flow model. The sequence is composed of 49 images with an average displacement in the streamwise direction of approximately 6 pixels. In Figure (5.8), we get to have a general idea of the sequence motion patterns by plotting the mean SGSD vector field. The 3D deformations mentioned earlier are readily noticeable when visualizing the dense vector field. SGSD was able to recover a better trajectory compared to other methods, Figure (5.9, top). Testing different Sc_t values other than the default value 1 showed similar performance for all variations until around the 20th image where the default SGSD showed better performance while SGSD with a larger diffusion coefficient gives a trajectory that diverges drastically to a bad local minimum with approximately 0.5 normalized error, Figure (5.9, bottom). Figure (5.10, left) shows the divergence field and the cross-section trajectories are plotted on the right in the same figure. One could see the effect of the aforementioned 3D motion on the highlighted rectangular area plotted on the trajectories.

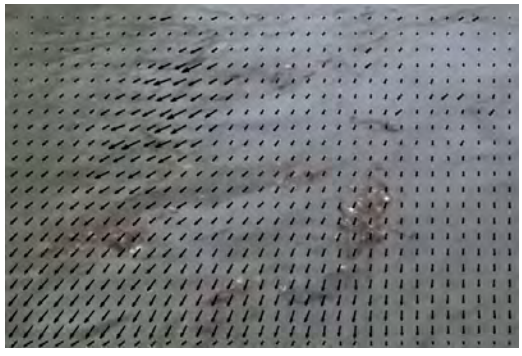

Figure 5.8: Mean dense SGSD velocity field of Gave de Pau sequence

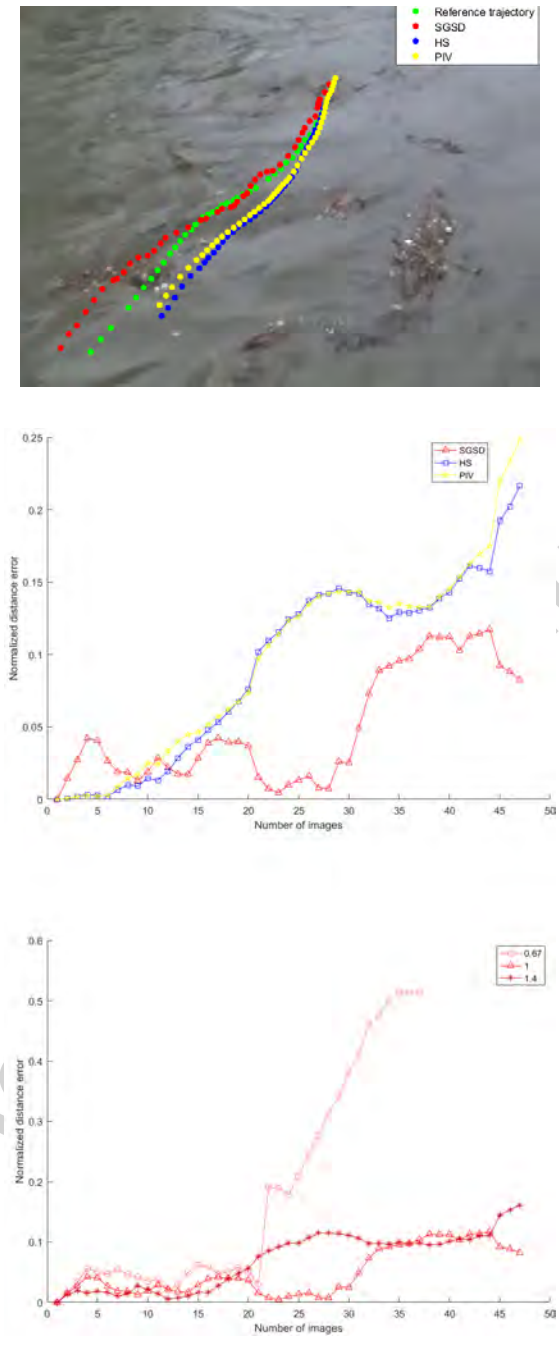

Figure 5.9: The trajectories of different methods superimposed on the first image of Gave de Pau river sequence (top), normalized distance error of different methods (middle) and the normalized distance error of SGSD with different turbulent Schmidt number (bottom)

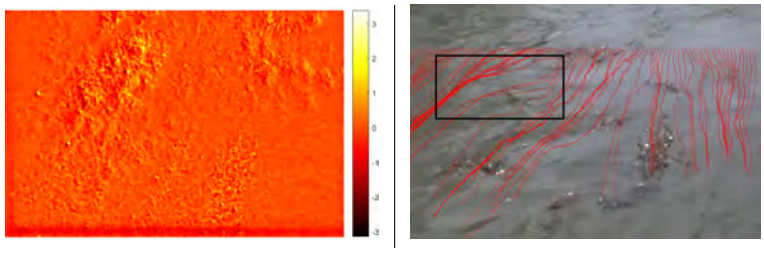

Figure 5.10: Other relevant quantities derived from SGSD for Gave de Pau sequence: divergence of the mean vector field (left). Trajectories on a cross-section (right)

5.2. Results on ortho-rectified images

In river velocimetry, LSPIV is the benchmark image-based method to estimate free surface velocity. It applies PIV to a grid of points defined in ortho-rectified images. Image ortho-rectification is a way to transform the image to remove the perspective effect so that a direct relationship between image space and the real world could be established, Figure (5.11). The resulting transformed sequence is used to compute river velocity using image-based techniques like PIV. Unfortunately, the philosophy of LSPIV is different from optical flow which makes the comparison difficult. LSPIV relies on estimations obtained on many images and use statistics (the mean mostly) to average the final flow field to reduce the effects of outliers. This makes trajectory reconstruction difficult because it uses successive individual estimations and only one outlier is enough to cause the whole trajectory to diverge. Optical flow is different in this regard as it integrates outlier rejection in the process (i.e. even between only two images) via median filtering and/or regularization. In addition, the interpolation step needed for trajectory reconstruction will be more accurate on optical flow since the interpolation is applied between image pixels themselves while in LSPIV one needs to interpolate between grid points that are many pixels apart, Figure(5.11, bottom). We used FUDAA-LSPIV software (Le Coz et al., 2014) to ortho-rectify the sequence and compute real world velocity on the defined grid. The sequence is extracted with 5 images per second frame-rate. We run SGSD on the ortho-rectified sequence, Figure (5.12) shows SGSD trajectory reconstruction in comparison to the manual reference trajectory. To compare SGSD to LSPIV, we superimpose the same LSPIV grid on SGSD dense field and compare velocity values only for grid points, Figure (5.13). Both methods give similar results. A noticeable difference is observed on the top and bottom sides of the grid. However, this is not surprising since estimations on image boundaries are known to be prone to errors. In addition, lower and upper part of images have no much tracers to rely on and they contain a fixed shadow pattern.

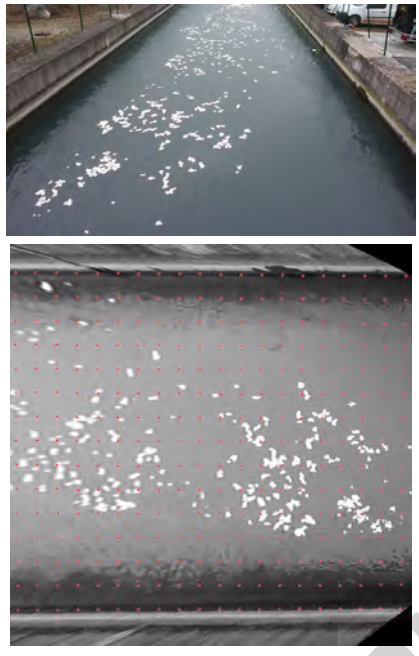

Figure 5.11: Original image (top), ortho-rectified image with grid points in red (bottom)

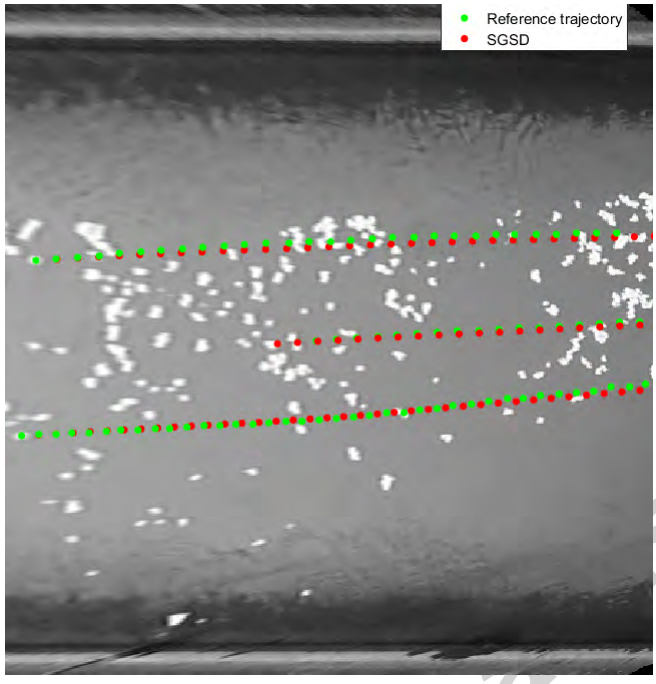

Figure 5.12: SGSD and manual trajectories superimposed on the first image of the ortho-rectified sequence

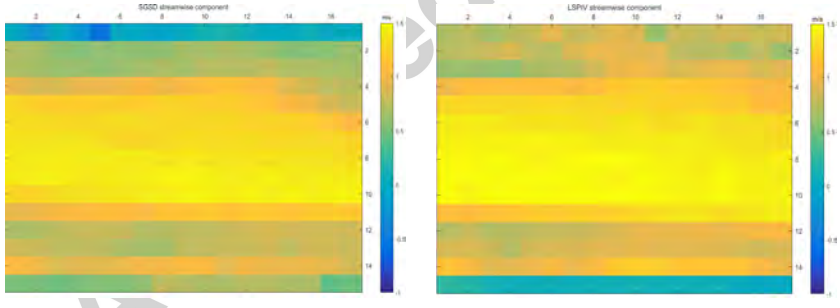

Figure 5.13: Real world velocity estimations on grid points, SGSD (left), LSPIV (right)

6. Conclusion

We presented a novel motion estimation technique for the application of image-based river velocimetry, based on optical flow scheme. We showed that optical flow in its own right is optimal and physically compatible with rivers free surface motions. In the ideal settings as in the first Arc sequence, section (5.1.1), original optical flow

provided very good results without any additional terms. Our enhanced model is based on the decomposition of the scalar transport equation which is equivalent to the original optical flow in addition to a new term. This term, considered to be related to turbulent viscosity, models the small scale contributions that are dropped out in the image acquisition phase. We suggested a turbulent diffusion coefficient based on *Prandtl* Mixing Length model and a Sc_t value of 1. This choice of Sc_t gave more stable results. Other values (bigger or smaller than 1) either gave less accurate results or good results at the beginning of the sequence but then drastically diverge with time. We presented results on different possible cases of rivers with or without tracers, good or poor imaging conditions, high or low surface velocity and high or low surface perturbations. Our method outperformed all other approaches in all image sequences in the recovered motion magnitude and/or direction. Both assessed visually or statistically via trajectory reconstruction of particles of interest. We draw the attention here to the sensibility of trajectory reconstruction to outliers, any wrong value at any instance of the estimated vector fields sequence will ruin the part of the trajectory that follows it. It is also sensitive to systematic errors that would accumulate in time to reconstruct erroneous trajectories. Nevertheless, we have been able to reconstruct trajectories that are similar to their reference trajectories. It is also shown how the dense estimation of optical flow facilitates the computation of other relevant quantities like divergence and vorticity fields. Since the application treated here mainly focuses on river velocimetry, our model is designed to penalize the vorticity of the vector field. However, the variational formulation is flexible and could open the door to more specialized optical flow models for complex river flows. In this case, new motion patterns will emerge that are different from the translatory pattern assumed in this paper. For example, a river flow around an object will introduce large-scale rotational motion pattern. The optical flow model could be easily changed to avoid the penalization of this quantity during the estimation process by using the regularization suggested by Chen et al. (2015). Using trajectory reconstruction evaluation method feedback, new data terms/regularizers and models for the diffusion coefficients could also be tested and assessed.

Acknowledgements

This work was supported by EDF-DTG and SCHAPI. Authors also would like to thank Jérôme Le Coz and Alexandre Hauet for their insightful comments on FUDAA-LSPIV software along with the LSPIV project used in section 5.2.

Adrian, R., Jan. 1991. Particle-Imaging Techniques for Experimental Fluid-Mechanics. Annual Review of Fluid Mechanics 23 (1), 261–304.

Baker, S., Scharstein, D., Lewis, J. P., Roth, S., Black, M. J., Szeliski, R., Mar. 2011. A Database and Evaluation Methodology for Optical Flow. International Journal of Computer Vision 92 (1), 1–31.

Bergen, J. R., Anandan, P., Hanna, K. J., Hingorani, R., May 1992. Hierarchical Model-Based Motion Estimation. In: Computer Vision — ECCV 92. Springer, Berlin, Heidelberg, pp. 237–252.

Black, M. J., Anandan, P., Jan. 1996. The Robust Estimation of Multiple Motions: Parametric and Piecewise-Smooth Flow Fields. Computer Vision and Image Understanding 63 (1), 75–104.

Blake, A., Zisserman, A., 1987. Visual Reconstruction. MIT Press.

Brox, T., Bruhn, A., Papenberg, N., Weickert, J., Jan. 2004. High Accuracy Optical Flow Estimation Based on a Theory for Warping. In: Computer Vision - ECCV 2004. Vol. 3024 of Lecture Notes in Computer Science. Springer Berlin Heidelberg, pp. 25–36.

Butler, D. J., Wulff, J., Stanley, G. B., Black, M. J., Oct. 2012. A Naturalistic Open Source Movie for Optical Flow Evaluation. In: European Conf. on Computer Vision (ECCV). Part IV, LNCS 7577. Springer-Verlag, pp. 611–625.

Carlier, J., Wieneke, B., 2005. Report 1 on Production and Diffusion of Fluid Mechanics Images and Data.

Cassisa, C., Simoens, S., Prinet, V., Shao, L., Dec. 2011. Subgrid Scale Formulation of Optical Flow for The Study of Turbulent Flow. Experiments in Fluids 51 (6), 1739–1754.

Charbonnier, P., Blanc-Feraud, L., Aubert, G., Barlaud, M., Nov. 1994. Two Deterministic Half-Quadratic Regularization Algorithms for Computed Imaging. In: Proceedings of 1st International Conference on Image Processing. Vol. 2. pp. 168–172 vol.2.

Chen, X., Zillé, P., Shao, L., Corpetti, T., Jan. 2015. Optical Flow for Incompressible Turbulence Motion Estimation. Experiments in Fluids 56 (1).

Corpetti, T., Heitz, D., Arroyo, G., Mémin, E., Santa-Cruz, A., Oct. 2005. Fluid Experimental Flow Estimation Based on an Optical-Flow Scheme. Experiments in Fluids 40 (1), 80–97.

Cui, G. X., Xu, C. X., Fang, L., Shao, L., Zhang, Z. S., Jul. 2007. A New Subgrid Eddy-Viscosity Model for Large-Eddy Simulation of Anisotropic Turbulence. Journal of Fluid Mechanics 582, 377–397.

Dramais, G., Le Coz, J., Camenen, B., Hauet, A., Dec. 2011. Advantages of a Mobile LSPIV Method for Measuring Flood Discharges and Improving Stage-Discharge Curves. Journal of Hydro-environment Research 5 (4), 301–312.

Fujita, I., Muste, M., Kruger, A., 1998. Large-Scale Particle Image Velocimetry for Flow Analysis in Hydraulic Engineering Applications. Journal of Hydraulic Research 36 (3), 397–414.

Gualtieri, C., Angeloudis, A., Bombardelli, F., Jha, S., Stoesser, T., Apr. 2017. On the Values for the Turbulent Schmidt Number in Environmental Flows. Fluids 2 (2), 17.

Heitz, D., Héas, P., Mémin, E., Carlier, J., Oct. 2008. Dynamic Consistent Correlation-Variational Approach for Robust Optical Flow Estimation. Experiments in Fluids 45 (4), 595–608.

Heitz, D., Mémin, E., Schnörr, C., Mar. 2010. Variational Fluid Flow Measurements from Image Sequences: Synopsis and Perspectives. Experiments in Fluids 48 (3), 369–393.

Horn, B. K. P., Schunck, B. G., Aug. 1981. Determining Optical Flow. Artificial Intelligence 17 (1–3), 185–203.

Jodeau, M., Hauet, A., Paquier, A., Coz, J. L., Dramais, G., 2008. Application and Evaluation of ls-piv Technique for the Monitoring of River Surface Velocities in High Flow Conditions. Flow Measurement and Instrumentation 19 (2), 117 – 127.

Khalid, M., Pénard, L., Mémin, E., Jul. 2017. Application of Optical Flow for River Velocimetry. In: 2017 IEEE International Geoscience and Remote Sensing Symposium. Fort-Worth, Texas, USA, pp. 6243–6246.

Le Coz, J., Jodeau, M., Hauet, A., Marchand, B., Le Boursicaud, R., 2014. Image-based Velocity and Discharge Measurements in Field and Laboratory River Engineering Studies Using the Free FUDAA-LSPIV Software. In: Proceedings of the International Conference on Fluvial Hydraulics, RIVER FLOW 2014. pp. 1961–1967.

Liu, C., Jun. 2009. Beyond Pixels: Exploring New Representations and Applications for Motion Analysis. Ph.D. thesis, Massachusetts Institute of Technology.

Liu, T., Shen, L., Nov. 2008. Fluid Flow And Optical Flow. Journal of Fluid Mechanics 614, 253–291.

Mémin, E., Pérez, P., Jan. 1998. A Multigrid Approach for Hierarchical Motion Estimation. In: Sixth International Conference on Computer Vision, 1998. pp. 933–938.

Mémin, E., Pérez, P., Feb. 2002. Hierarchical Estimation and Segmentation of Dense Motion Fields. International Journal of Computer Vision 46 (2), 129–155.

Muste, M., Hauet, A., Fujita, I., Legout, C., Ho, H.-C., 2014. Capabilities of Large-Scale Particle Image Velocimetry to Characterize Shallow Free-Surface Flows. Advances in Water Resources 70, 160 – 171.

Patalano, A., Garc C. M., Rodrez, A., 2017. Rectification of image velocity results (RIVeR): A simple and user-friendly toolbox for large scale water surface particle image velocimetry (PIV) and particle tracking velocimetry (PTV). Computers & Geosciences 109, 323 – 330.

Piccinini, F., Kiss, A., Horvath, P., Mar. 2016. CellTracker (not only) for dummies. Bioinformatics 32 (6), 955–957.

Prandtl, L., 1925. Z. angew. Math. Mech. 5 (1), 136–139.

Ray, N., Oct. 2011. Computation of Fluid and Particle Motion From a Time-Sequenced Image Pair: A Global Outlier Identification Approach. IEEE Transactions on Image Processing 20 (10), 2925–2936.

Sun, D., Roth, S., Black, M., 2014. A Quantitative Analysis of Current Practices in Optical Flow Estimation and the Principles Behind Them. International Journal of Computer Vision 106 (2), 115–137.

Suter, D., Jun. 1994. Motion Estimation and Vector Splines. In: , 1994 IEEE Computer Society Conference on Computer Vision and Pattern Recognition, 1994. Proceedings CVPR '94. pp. 939–942.

Tominaga, Y., Stathopoulos, T., 2007. Turbulent Schmidt Numbers for CFD Analysis with Various Types of Flowfield. Atmospheric Environment 41 (37), 8091 – 8099.